J. Indian Inst. Sci., Jan.–Feb. 1996, 76, 37–57.

Mixed-mode ductile fracture initiation

R. NARASIMHAN AND A. K. GHOSAL
Department of Mechanical Engineering, Indian Institute of Science, Bangalore 560 012, India .

Received on September 5, 1995.

Abstract

In this paper, an overview of some recent computational studies by the authors on mixed-mode ductile fracture initiation is presented. In these studies, mixed-mode ductile fracture involving Modes I and II was analyzed using the finite-element procedure within the context of plane strain, small-scale yielding conditions. The main objective of these analyses was to investigate the micro-mechanics of mixed-mode ductile fracture. To this end, the finite strain version of the Gurson constitutive model which represents the ductile failure processes of micro-void nucleation, growth and coalescence was employed. The numerical simulations were carried out in three parts. In the first, ductile fracture initiation from a notch under mixed-mode loading was analyzed. In the second, the effect of initiation of a discrete void by inclusion debonding and its interaction with a nearby notch tip was studied. In the third, porosity development due to a rectangular distribution of *synthetic inclusions* around the notch tip was modelled. Some important results from the above simulations are presented here and are compared with available experimental observations.

Keywords: Ductile fracture, mixed-mode loading, micro-void coalescence, shear localization.

1. Introduction

Structural components are often subjected to complex loading which will result in mixed-mode fracture (involving Modes I, II and III) at the tip of an existing crack or notch. Thus, in order to have guidelines for improving the safety design of a structural component, as well as for proper material selection, it is important to have a clear understanding of the issues connected with mixed-mode fracture. These issues include the fundamental micro-mechanical processes involved in fracture initiation and the effect of mode-mixity on the fracture toughness, stability and direction of crack propagation. The present paper is concerned with the first two issues mentioned above within the context of ductile materials.

Ductile fracture occurs on the microscale mainly by nucleation, growth and coalescence of voids. The nucleation of voids in engineering alloys takes place by brittle cracking or interfacial decohesion of inclusions or second-phase particles. This is followed by the growth of the voids which is caused by plastic deformation in the surrounding material and is influenced by high triaxial tension. It has been observed (see, for example, Cox and Low[1] and Hahn and Rosenfield[2]) that in structural materials, such as steels and aluminum alloys, void initiation can involve two distinct populations of inclusions of vastly different sizes. In such materials, voids initiate first at the large weak

particles, and after growing to some size they coalesce, or link up with a nearby notch tip, *via* a *void sheet* consisting of voids nucleated from a second population of small size particles. The formation of the void sheet is triggered by concentration of plastic strain in the ligament connecting two large scale voids or that connecting a large scale void with a nearby notch tip.

In recent years, several investigators (Otsuka *et al.*[3], Tohgo *et al.*[4], Aoki *et al.*[5], Maiti and Mahanty[6] and Maccagno and Knott[7]) have studied experimentally mixed-mode ductile fracture in steels and aluminum alloys. Their results show that under mixed-mode loading, one portion of the notch surface blunts while the remaining portion sharpens. Further, it is observed from detailed metallographic investigations (see, for example, Tohgo *et al.*[4]) that for Mode I predominant mixed-mode loading, fibrous-type crack initiation occurs by coalescence of micro-voids at the blunted part of the notch. On the other hand, for Mode II, predominant mixed-mode loading, shear-type crack initiation occurs due to large shear deformation at the sharpened part of the notch. Thus, there are two competing mechanisms (micro-void coalescence and shear band formation) during ductile failure near a notch tip under mixed-mode loading. However, contrasting trends have been reported in the literature regarding the effect of mode-mixity on the fracture toughness which could be, for example, the value of the J integral (Rice[8]) at initiation of ductile failure near the notch tip. Thus, while the experimental results of Tohgo *et al.*[4] and Maiti and Mahanty[6] show a decrease in J for change in loading from Mode I to Mode II, the reverse trend is observed for the materials considered by Aoki *et al.*[5] and Maccagno and Knott [7].

The complex micro-mechanical processes mentioned above and the factors responsible for observed macroscopic behaviour, like the dependence of fracture toughness on mode-mixity, can be well understood through careful numerical simulations which model the local failure processes near a crack tip. To this end, a series of finite-element studies was undertaken by the authors[9-11] to investigate the micro-mechanics of mixed-mode ductile fracture involving Modes I and II. In this paper, an overview of the salient contributions of the above studies is presented. In all the investigations cited above, the Gurson[12] constitutive model, which accounts for micro-void nucleation, growth and coalescence, was employed and the computations were performed within the framework of a 2D plane strain, finite deformation theory. Attention was restricted to small-scale yielding conditions. A brief description of the above constitutive model is given in Section 2.

Ghosal and Narasimhan[9] performed finite-element analyses of mixed-mode ductile fracture initiation from a notch. They simulated the initiation and propagation of the micro-void damage zone through the finite-element mesh. Also, they employed a critical plastic strain criterion to identify the formation of the shear crack at the sharpened part of the notch for loading with a high Mode II component. The important results from their work are presented in Section 3.1.

The above numerical study assumed that void nucleation occurs only at small size particles (much less than, say, 1 μm in size) which are uniformly dispersed in the ma-

trix. However, as already mentioned, microstructural investigations show that two distinct populations of void nucleating particles of vastly different sizes are present in many engineering alloys. As a first step towards understanding mixed-mode fracture in such materials, Ghosal and Narasimhan[10] analyzed the effect of initiation of a large void (comparable in size to the notch diameter) by inclusion debonding, its subsequent growth, and final coalescence with the notch tip (*via* a void sheet). They chose a simple constitutive model to represent the interface between a large size, rigid inclusion situated ahead of a notch tip and the surrounding metal matrix. From the above analysis, they studied the formation and growth of the hole, and the failure of the ligament connecting the notch tip with the hole by either micro-void coalescence or by shear crack propagation. Some salient results from their work are presented in Section 3.2.

Although the above analysis provided important insight into the physical processes involved during mixed-mode ductile fracture when two size scales of particles are present, a *distribution* of large discrete particles was not modelled. Hence, Ghosal and Narasimhan[11] conducted finite-element simulations with the view of studying the mixed-mode ductile fracture mechanisms taking into account void initiation at a dual distribution of particles (of different sizes). The initiation of voids at small, uniformly distributed particles was assumed to be based on a strain-controlled mechanism. On the other hand, a stress-controlled void nucleation law was used within the framework of the Gurson constitutive model to simulate voids at large inclusions. Thus, unlike Ghosal and Narasimhan[10], the large inclusions were not modelled explicitly. Instead, a rectangular distribution of *synthetic inclusions* around the notch tip was considered. This technique was introduced in a previous work by Narasimhan[13].

Ghosal and Narasimhan[11] focussed attention on the formation of porosity around the synthetic particles, their growth and eventual link up with the notch tip under mixed-mode loading. Also, the effect of mode mixity on the critical value of J associated with complete failure of the ligament bridging the notch tip and the nearest large particle (which is taken to signify fracture initiation) was investigated. A possible mechanism for the contrasting experimental trends reported in the literature regarding this issue was identified. The most important results from their work are given in Section 3.3.

2. Constitutive model

In the studies undertaken by Ghosal and Narasimhan[9–11], the constitutive equations proposed by Gurson[12], which are based on a continuum elastic-plastic model that accounts for micro-void nucleation and growth, were employed. This model was subsequently modified by Tvergaard and Needleman[14], since in its original form the complete loss of material stress-carrying capacity due to micro-void coalescence was not predicted at a realistic level of void volume fraction. The modified Gurson yield condition which depends on the macroscopic (aggregate) Cauchy stress σ_{ij}, the microscopic (matrix) tensile flow stress σ_m, and the current void volume fraction f is given by:

$$\Phi(\sigma_{ij},\sigma_m,f)=\frac{\sigma_e^2}{\sigma_m^2}+2f^*q_1\ \cosh\left(\frac{3\sigma_H}{2\sigma_m}\right)-\left(1+(q_1f^*)^2\right)=0. \tag{1}$$

It should be noted that the above yield condition depends both on the deviatoric component S_{ij} of the Cauchy stress tensor through the macroscopic equivalent stress $\sigma_e = (3/2\, S_{ij}S_{ij})^{1/2}$ and also on the hydrostatic stress $\sigma_H = \sigma_{kk}/3$. This model thus exhibits a dilatational plastic behaviour which is an outcome of the presence of micro-voids inside the matrix. Tvergaard[15] introduced the parameter q_1 in eqn (1), with a value of 1.5, to obtain better agreement between predictions of this model and numerical studies of periodic array of voids.

The modelling of final material failure by micro-void coalescence is accomplished through the function $f^*(f)$ in eqn (1) which is defined by:

$$f^* = \begin{cases} f & f \le f_c \\ f_c + K(f - f_c) & f > f_c, \end{cases} \tag{2}$$

where $K = (1/q_1 - f_c)/(f_F - f_c)$. Here, f_c is the value of the void volume fraction at which void coalescence first occurs and f_F is its value at final failure. From the above equation, it is clear that as $f \to f_F$, $f^* \to f_u^* = 1/q_1$. Further, it can be observed from the yield condition (1) that the material loses its stress-carrying capacity, when $f^* \to f_u^* = 1/q_1$. Thus, an essential feature of the model is that a failure criterion is directly built into the constitutive equations. Experimental studies (see, for example, Cox and Low[1]) indicate that the ligament connecting two neighbouring voids fails by shear band formation or by simple necking when the size of the voids has grown to the order of magnitude of their spacing. An estimate of f_c obtained by Brown and Embury[16] from a simple model is 0.15. Also, a numerical investigation by Andersson[17] suggests that $f_F \approx 0.25$.

The response of the matrix material in uniaxial tension is idealized by a piecewise power-hardening law of the form:

$$\frac{\varepsilon_m}{\varepsilon_0} = \begin{cases} \sigma_m/\sigma_0 & \sigma_m \le \sigma_0 \\ (\sigma_m/\sigma_0)^n & \sigma_m > \sigma_0. \end{cases} \tag{3}$$

Here, σ_0 is the initial yield stress and $\varepsilon_0 = \sigma_0/E$ is the initial yield strain of the matrix material. In all the computations reported here, ε_0 was chosen as 0.002. Further, unless otherwise stated, the value of the strain-hardening exponent n was taken as 10.

The void volume fraction f is allowed to evolve both due to growth of existing voids and nucleation of new voids, so that,

$$\dot{f} = \dot{f}_{\text{growth}} + \dot{f}_{\text{nucleation}}. \tag{4}$$

The growth law, which is described by,

$$\dot{f}_{\text{growth}} = (1 - f)D_{kk}^P, \tag{5}$$

where D^p_{nn}, the plastic part of the rate of deformation, is an outcome of the plastic incompressibility of the matrix material. It should, however, be noted that the macroscopic material response does not satisfy plastic incompressibility due to the existence of voids.

Gurson[18] has discussed various void nucleation models. The particular type that is used in this work is of the form:

$$\dot{f}_{\text{nucleation}} = \mathcal{A}\,\dot{\varepsilon}^p_m + \mathcal{B}(\dot{\sigma}_m + c\dot{\sigma}_{II}), \tag{6}$$

which was proposed by Needleman and Rice[19]. In this equation, c is a constant less than unity and $\mathcal{A}(\cdot)$ and $\mathcal{B}(\cdot)$ are considered as functions of ε^p_m and $\sigma_m + c\,\sigma_{II}$, respectively. The choice of these functional forms is discussed below.

A plastic strain-controlled void nucleation law can be employed (see Thomason[20]) to model void nucleation at small particles (less than 1 μm in size) which can be assumed to be uniformly distributed in the matrix. In this case, the function $\mathcal{B} \equiv 0$, and the function $\mathcal{A}(\varepsilon^p_m)$ is chosen as (see Chu and Needleman[21]):

$$\mathcal{A} = \frac{f_n}{s_n\sqrt{2\pi}} \exp\left[-\frac{1}{2}\left(\frac{\varepsilon^p_m - \varepsilon_n}{s_n}\right)^2\right], \tag{7}$$

so that void nucleation follows a normal distribution about a mean nucleation strain ε_n with standard deviation s_n. In the above equation, f_n denotes the volume fraction of void nucleating particles which initiate voids by a plastic strain-controlled mechanism. In all the computations reported here, $f_n = 0.04$, $\varepsilon_n = 0.3$ and $s_n = 0.1$ were employed.

In order to represent micro-void nucleation at large size inclusions (greater than about 1 μm), a model based on the maximum normal stress at the particle-matrix interface should be used. This idea has been suggested by the works of Argon *et al.*[22] (see also Thomason[20]). The above mechanism can be represented through the nucleation law (6) by taking the function $\mathcal{A} \equiv 0$ and by choosing the function $\mathcal{B}(\sigma_m + c\sigma_{II})$ to have a normal distribution about a mean nucleation stress σ_N so that:

$$\mathcal{B} = \frac{\hat{f}_n}{\hat{s}_n\sqrt{2\pi}} \exp\left[-\frac{1}{2}\left(\frac{(\sigma_m + c\sigma_{II}) - \sigma_N}{\hat{s}_n}\right)^2\right], \tag{8a}$$

for

$$(\sigma_m + c\sigma_{II}) = (\sigma_m + c\sigma_{II})_{\max} \text{ and } (\dot{\sigma}_m + c\dot{\sigma}_{II}) > 0. \tag{8b}$$

Here, $\hat{f}_n$ is the volume fraction of particles that initiate voids by the mechanism described above which is based on the interface stress, and $\hat{s}_n$, a standard deviation about the mean nucleation stress σ_N. If the condition (8b) is violated then $\mathcal{B}$ is taken as zero. The value of c was taken as 0.6 to account for partial conversion of the remote hydrostatic stress into local shearing stress around the inclusion.

The above constitutive equations were employed within the framework of a finite deformation theory of plasticity with small elastic strains (see Ghosal[23] for a full description). The details of the finite deformation finite-element procedure used in the computations reported here may also be found in Ghosal[23].

As noted above, complete loss of material stress-carrying capacity occurs when $f^* = f_u^* = 1/q_1$ (or equivalently when $f = f_F$) resulting in local material failure. This implies that the material completely separates at this point and a traction-free surface develops. This failure criterion was implemented in the numerical procedure by freezing the evolution of f (see Tvergaard[24]) after it reaches a value close to f_F (around $0.95\,f_F$). The macroscopic material response is then elastic-perfectly plastic with a small pressure-dependent yield stress. The condition $f = 0.95\,f_F$ was used instead of $f = f_F$ because as $f \to f_F$, the macroscopic equivalent stress $\sigma_e \to 0$, causing numerical difficulties.

3. Results and discussion

3.1 *Mixed-mode ductile fracture at a notch tip*

In this section, some results from a 2D plane strain finite-element analysis of mixed-mode ductile fracture initiation from a notch tip under small-scale yielding (Ghosal and Narasimhan[9]) are presented. Attention is focussed on two different failure mechanisms, involving micro-void coalescence and localized plastic deformation in the form of an intense band, which are simultaneously operating near the notch tip under mixed-mode loading. Only strain-controlled micro-void nucleation (see first term in right-hand side of eqn.(6)) was considered in these computations.

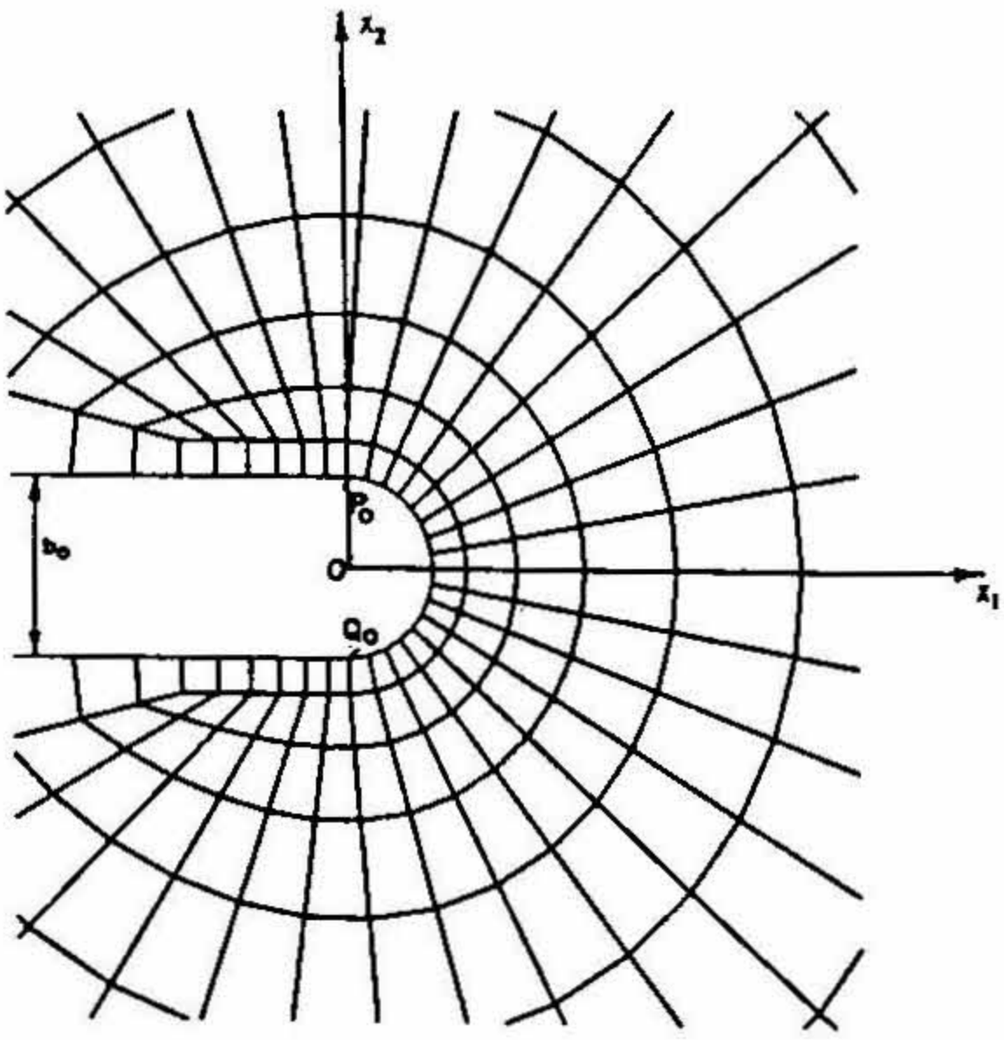

FIG. 1. Finite-element mesh used near the notch tip in analyses of mixed-mode ductile fracture initiation under small-scale yielding.

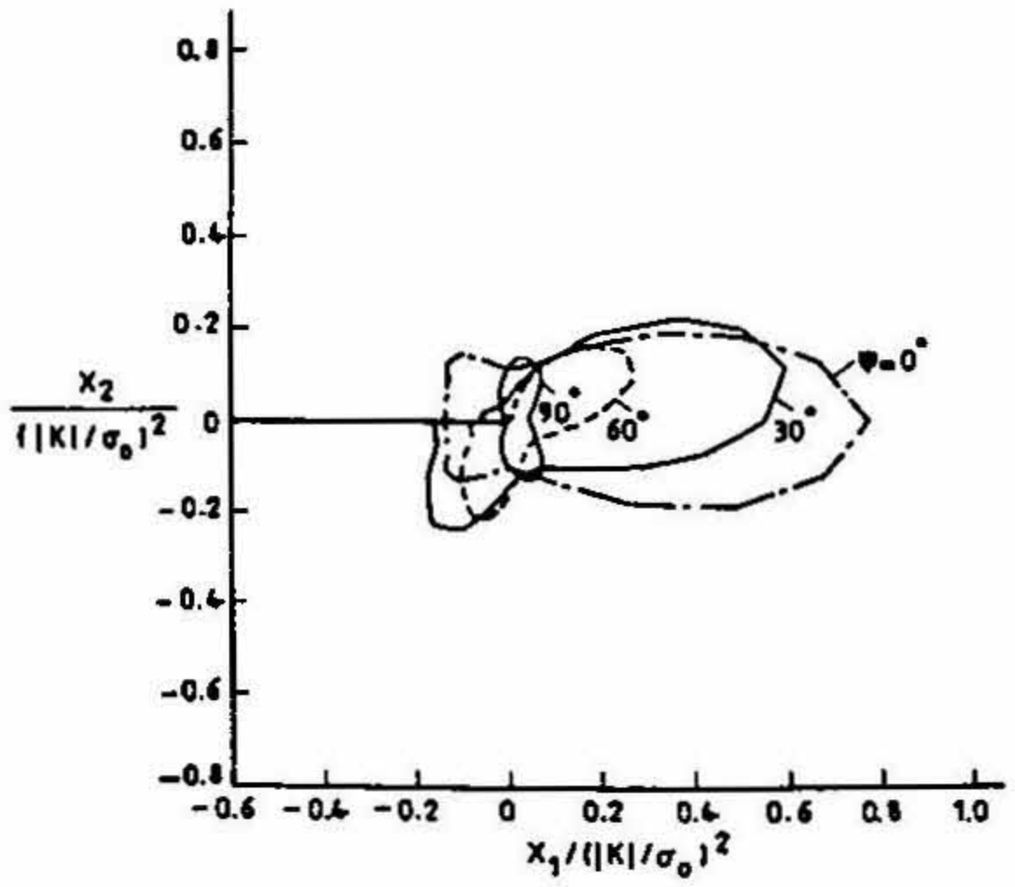

FIG. 2. Plastic zones in normalized (self-similar) co-ordinates for various levels of mode-mixity.

The plane-strain mixed-mode small-scale yielding problem (Rice[25]) was modelled by considering a circular domain containing a notch along one of its radii, which was entirely represented by isoparametric four-noded quadrilateral elements. The displacement vector corresponding to the mixed-mode elastic K-field, involving the Modes I and II stress-intensity factors, K_I and K_{II}, (see Rice[25]) was specified as boundary condition on the outermost boundary of the circular domain. The details of the refined mesh near the notch tip is shown in Fig.1. Here, the initial notch diameter is denoted by b_o and its centre of curvature O coincides with the centre of the circular domain. The simulations were carried out for various fixed values of the mode-mixity parameter $\psi = \tan^{-1}(K_I/K_{II})$ by increasing the magnitude of $|K| = \sqrt{K_I^2 + K_{II}^2}$. In the following, the load level will be expressed through the normalized parameter $J/(\sigma_0 b_0) = |K|^2(1-\nu^2)/(E\sigma_0 b_0)$, where J is Rice's[8] J integral. The maximum extent of the plastic zone surrounding the notch tip was at all times contained within 1/20 of the radius of the outermost boundary of the circular domain, to ensure that small-scale yielding conditions were preserved.

The plastic zones for four cases of mode-mixity are displayed in Fig. 2 using normalized Cartesian coordinates $x_1/(|K|/\sigma_0)^2$ and $x_2/(|K|/\sigma_0)^2$. The plastic zones are self-similar with respect to these axes. It can be seen from this figure that for Mode I ($\psi = 90°$), the plastic zone spreads more above and below the crack tip. On the other hand, with increasing Mode II component (decreasing ψ), the plastic zone spreads more ahead of the tip (in the x_1 direction). Further, the maximum size of the plastic zone increases dramatically as ψ changes from 90° (Mode I) to 0° (Mode II).

The deformed near-tip mesh for the mixed-mode case $\psi = 30°$ corresponding to a value of the normalized loading parameter $J/(\sigma_0 b_0) = 3.45$ is shown in Fig. 3. It can be seen from this figure that the top portion of the notch surface sharpens, while the bottom part blunts. The elements marked as 'x' have experienced complete material failure due to micro-void coalescence. In other words, the void volume fraction, f, in these elements has attained the preset failure limit of $0.95\, f_F$. It can be seen that these elements have stretched and enlarged considerably indicating that they have lost their stress-carrying capacity. Further, it should be noted that material failure due to micro-void coalescence has occurred near the blunted part of the notch surface.

The points P and Q in these figures indicate the locations on the deformed notch surface of the points marked as P_0 and Q_0 which are above and below the centre of the curvature of the notch root in the undeformed configuration (see Fig. 1). The linear distance d between points P and Q in Fig. 3 is a measure of the notch tip deformation. The variation of d/b_0 with the normalized loading parameter $J(\sigma_0 b_0)$ is shown in Fig. 4 for four cases of mode-mixity. The stage of loading at which incipient material failure (by micro-void coalescence) occurred near the notch tip is indicated in this figure. It can be seen from this figure that for a given value of $J(\sigma_0 b_0)$, the normalized notch tip deformation length d/b_0 increases as ψ is reduced from 90° and is maximum for $\psi = 30°$. The curves shown in Fig. 4 compare well with approximate estimates based on the mixed-mode asymptotic HRR tables given by Symington *et al.*[26] (see Appendix B of Ghosal[23]).

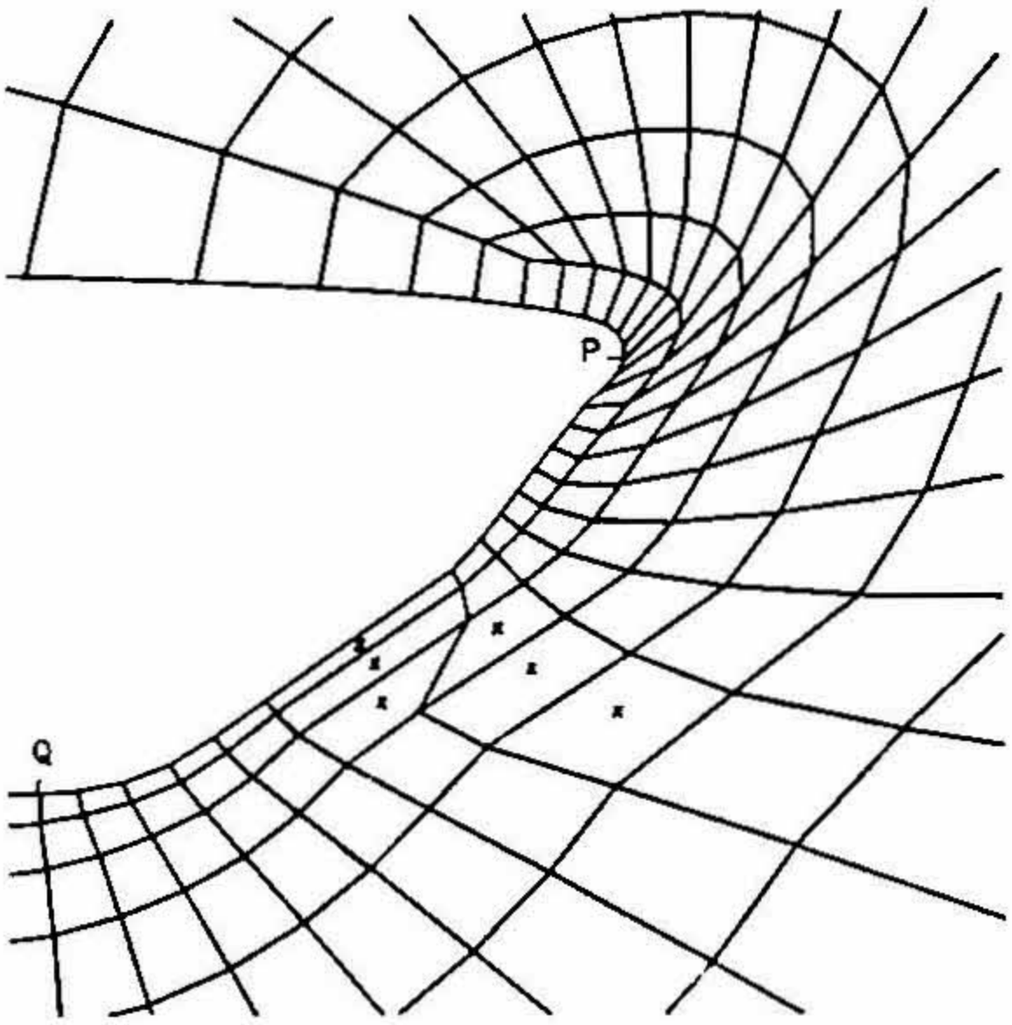

FIG. 3. Deformed mesh near the notch tip for $\psi = 30°$ at $J/(\sigma_0\, b_0) = 3.45$ ($d/b_0 = 3.67$). The failed elements are marked with x.

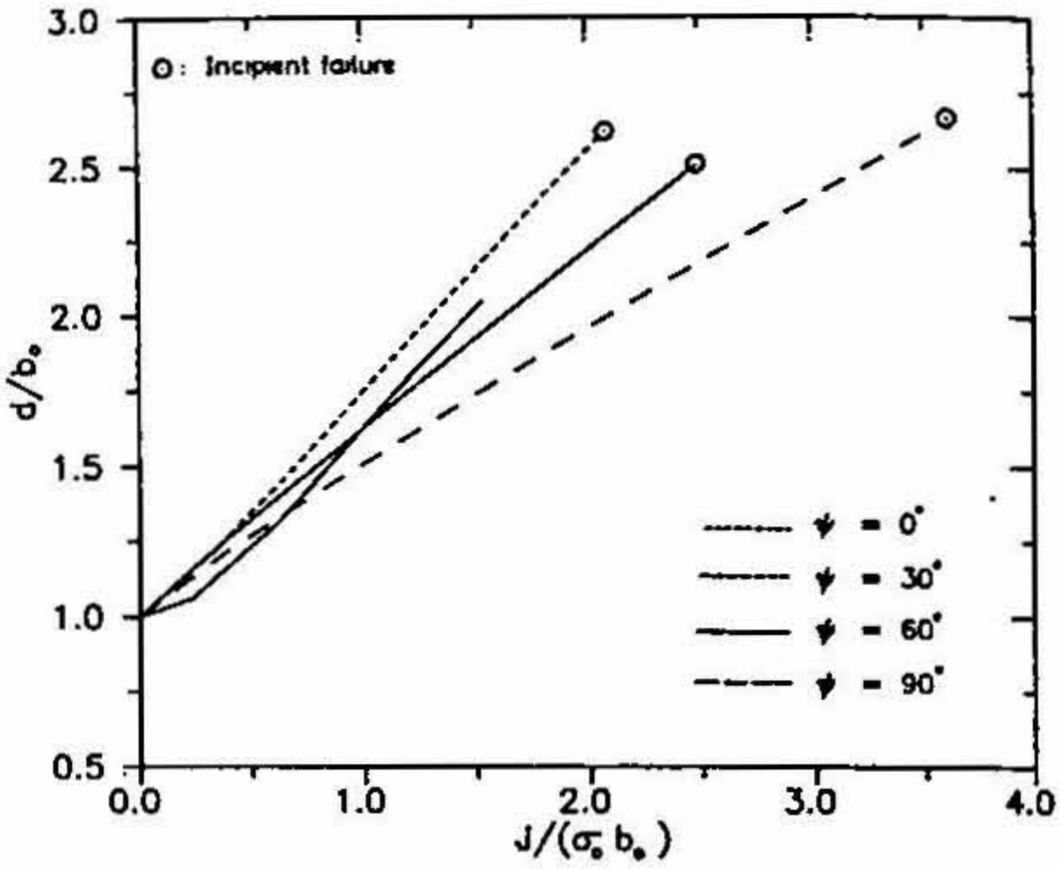

FIG. 4. Variation of normalized notch tip deformation length d/b_0 with normalized loading parameter $J/(\sigma_0\, b_0)$ for four cases of mode-mixity.

It can be observed from Fig. 4 that the value of d/b_0 at incipient material failure lies in the narrow range 2.4–2.7 and is practically independent of the extent of mixing of the two modes. As pointed out by Ghosal and Narasimhan[9], the reason for the above behaviour is due to a similarity between the curves shown in Fig. 4 and the evolution history of void volume fraction in the element near the notch tip that experienced incipient material failure. The above observation is supported by the experimental data of Tohgo *et al.*[4] for a structural steel SM41A. Their results show that for the above steel (which has very high strain hardening with $n \approx 3$), d/b_0 at fracture initiation due to micro-void coalescence is almost a constant with a value of around 3.0 for ψ ranging from 30° to 90°. Thus, the notch tip deformation length can be viewed as a *local* parameter for characterizing material failure by micro-void growth and coalescence near a notch tip under mixed-mode loading.

The contours of normalized hydrostatic stress $\sigma_H \backslash \sigma_0 = \sigma_{kk}/(3\sigma_0)$ near the notch tip in the deformed configuration are presented in Figs 5a and b for $\psi = 90°$ and 30° at a value of loading parameter $J/(\sigma_0\, b_0) = 3.4$ and 1.9, respectively. It is important to examine the contours of hydrostatic stress carefully because a large tensile hydrostatic stress promotes the growth of micro-voids. Firstly, it should be noted on comparing Figs 5a and b, that the orientation of the hydrostatic stress contours gets rotated clockwise (*i.e.*, towards the blunted part of the notch surface) as ψ decreases from 90°. The hydrostatic stress near the sharpened part of the notch in Fig. 5b is small. In fact, it becomes negative in this region (counter-clockwise with respect to contour A in Fig. 5b). In other words, a state of hydrostatic compression prevails in this region. Secondly, the magnitude of the hydrostatic stress near the notch tip decreases as ψ decreases from 90°. Thus, the peak value of σ_H in Figs 5a and b is $3\sigma_0$ and $1.7\sigma_0$ for $\psi = 90°$ and 30°, respectively.

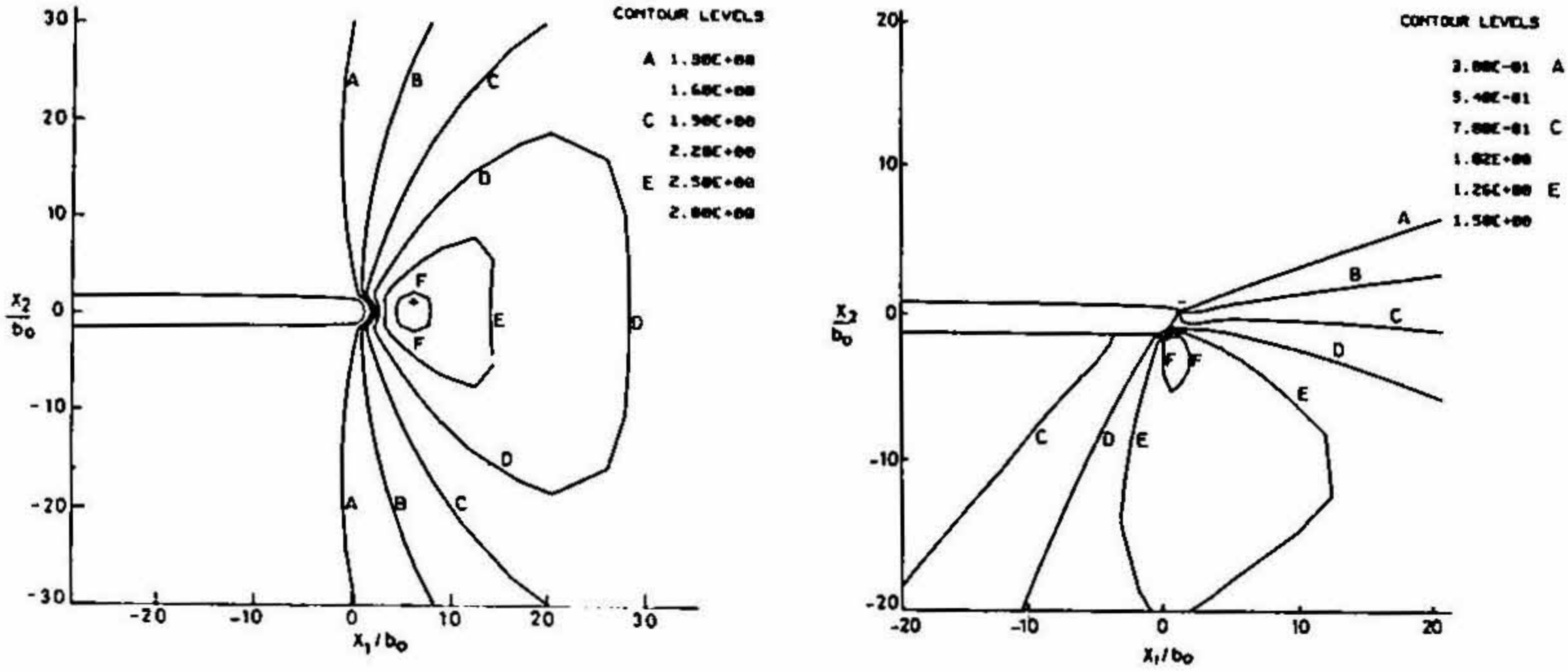

FIG. 5a. Contours of normalized hydrostatic stress σ_H/σ_0 for $\psi = 90°$ at $J/(\sigma_0 b_0) = 3.4$. b. Contours of normalized hydrostatic stress σ_H/σ_0 for $\psi = 30°$ at $J/(\sigma_0 b_0) = 1.9$.

The contours of void volume fraction around the notch tip in the deformed configuration for $\psi = 30°$ at $J/(\sigma_0 b_0) = 3.45$ are shown in Fig. 6. The length scale in this figure and in other contour plots to be presented later is set by the linear distance d between points P and Q. The value of $d = 3.67\ b_0$ at the stage of loading corresponding to Fig. 6. It can be seen from this figure that the maximum void volume fraction occurs adjacent to the blunted part of the deformed notch surface. By contrast, the level of void volume fraction near the sharpened part of the notch (see region adjacent to point P in Fig. 6) is small. This is due to the fact that the hydrostatic tensile stress is very small (see Fig. 5b) adjacent to the sharpened part of the notch which precludes the growth of micro-voids. The above observation is in accord with the experimental micrographs presented by Otsuka *et al.*[3] for ductile failure under Mode II, which clearly show the presence of large voids only near the blunted part of the notch as in Fig. 6.

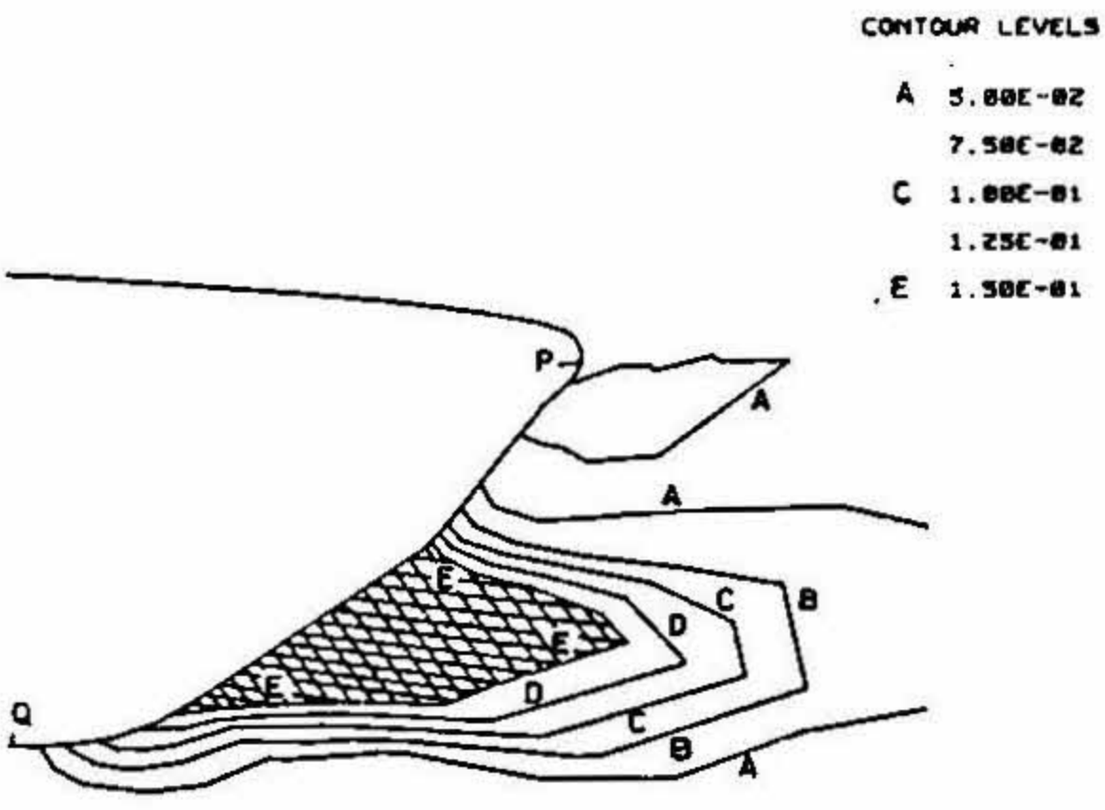

FIG. 6. Contours of void volume fraction f near the notch tip for $\psi = 30°$ at $J/(\sigma_0 b_0) = 3.45$ ($d/b_0 = 3.67$).

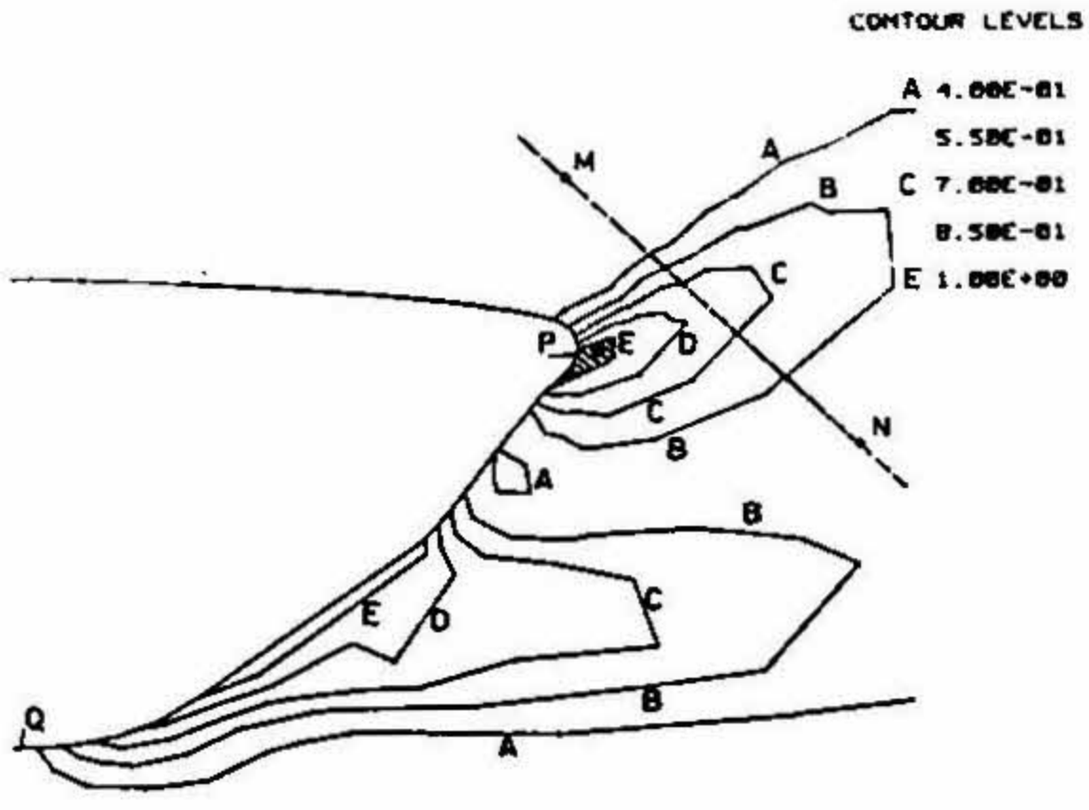

FIG. 7. Contours of matrix plastic strain ε'_m near the notch tip for $\psi = 30°$ at $J/(\sigma_0 b_0) = 3.45$ ($d/b_0 = 3.67$).

The hatched region enclosed between the deformed notch surface and the innermost contour E in Fig. 6 is the *micro-void damage zone*. Thus, for the material inside this damage zone, $f > f_c$, and it is close to complete material failure. It must be noted that failed elements marked by 'x' in Fig. 3 are within the damage zone indicated in Fig. 6. Further, the above damage zone strongly resembles the incipient fibrous crack from the blunted part of the notch surface observed by Tohgo *et al.*[4] in their mixed-mode fracture experiments.

The contours of matrix plastic strain in a detailed region surrounding the deformed notch are shown in Fig. 7 at $J/(\sigma_0 b_0) = 3.45$ ($d/b_0 = 3.67$) for the mixed-mode case $\psi = 30°$. It can be observed from this figure that large plastic strain has developed both adjacent to the blunted as well as the sharpened part of the notch. However, it is seen from Fig. 7 that the contours of ε_m^p near point P emanate in the form of a band from the sharpened portion of the notch surface. In other words, there is a large gradient of ε_m^p within the band of contours near point P. This can be understood by examining the variation of ε_m^p along the line MN which has been drawn across this band in Fig. 7. The above observation is corroborated by the large distortion (involving localized shearing and rotation) of elements emanating from point P in Fig. 3.

The material inside the above noted band of intense plastic strain concentration in Fig. 7 can also experience failure by the propagation of a shear crack which has been observed in the experiments of Tohgo *et al.*[4] for cases in which the Mode II component is very high. If it is tentatively assumed that failure would occur inside the strain concentration band if ε_m^p exceeds a critical value (of, say, 1.0), then the material shown hatched in Fig. 7 is likely to experience material failure. It is interesting to note that this strongly resembles the incipient shear crack observed by Tohgo *et al.*[4] in their experimental work.

Thus, the results presented in this section clearly show that two competing failure mechanisms involving micro-void coalescence and shear localization are operative near a notch tip in a ductile material under mixed-mode loading.

3.2 *Effect of void initiation and growth on mixed-mode ductile fracture*

As mentioned in the introduction, microstructural investigations (Cox and Low[1] and Hahn and Rosenfield[2]) show that two distinct populations of void nucleating particles of vastly different sizes are present in many engineering alloys. Hence, in order to understand ductile fracture initiation in such materials, it is imperative to study the interaction between the notch tip and a discrete void which has nucleated by interface debonding around a nearby large inclusion and the failure of the ligament connecting them. To this end, some results from the work of Ghosal and Narasimhan[10], wherein the above study was conducted, are presented in this section. As in Section 3.1, the finite-element analyses reported here were performed within the context of plane strain, small-scale yielding conditions.

The details of the refined mesh near the notch tip used in these simulations is shown in Fig. 8. At a distance $L_0 = 5\ b_0$ ahead of the notch tip, a circular (cylindrical) inclusion

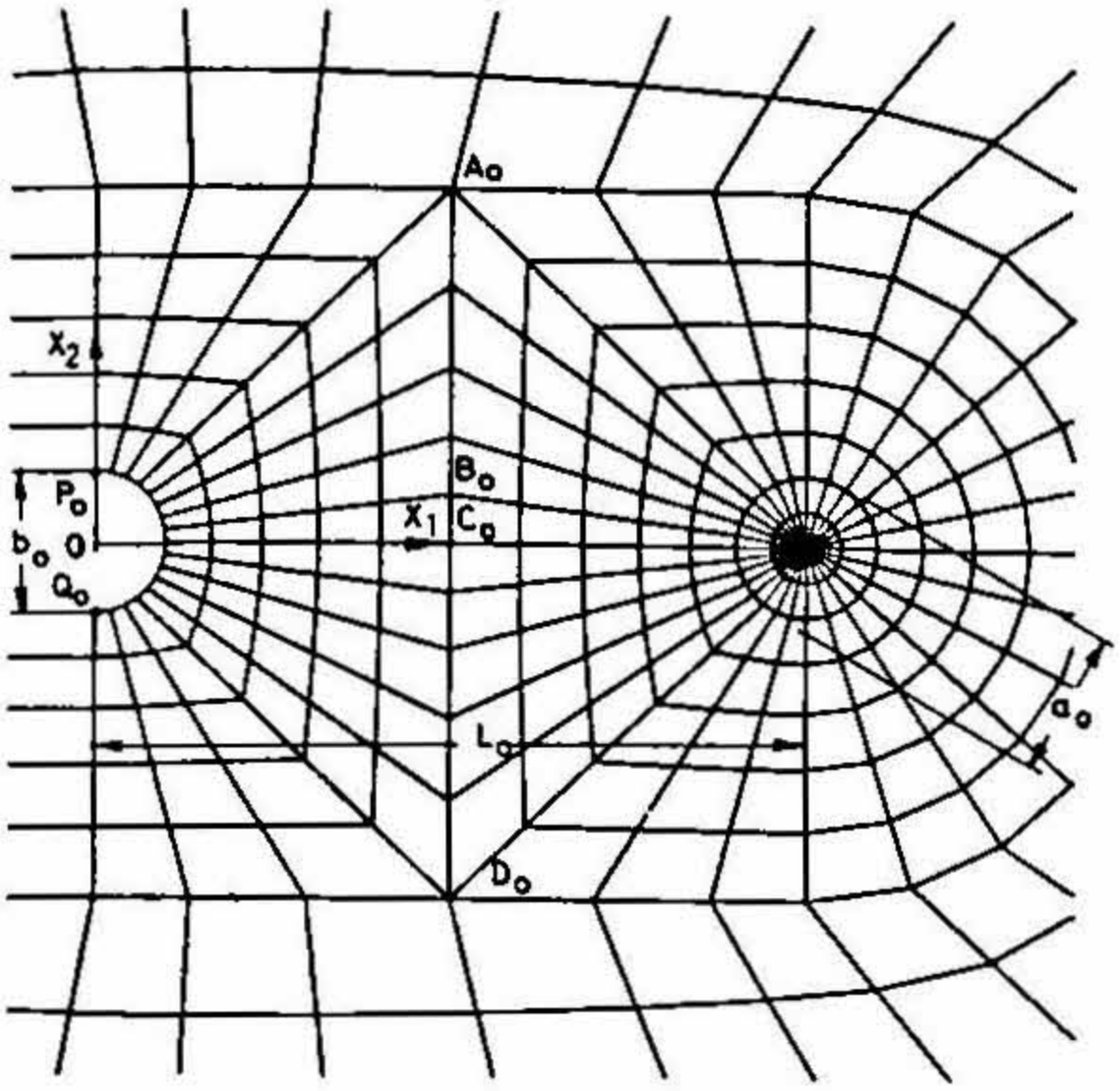

FIG. 8. Finite-element mesh showing the region near the notch tip and the inclusion ahead of it.

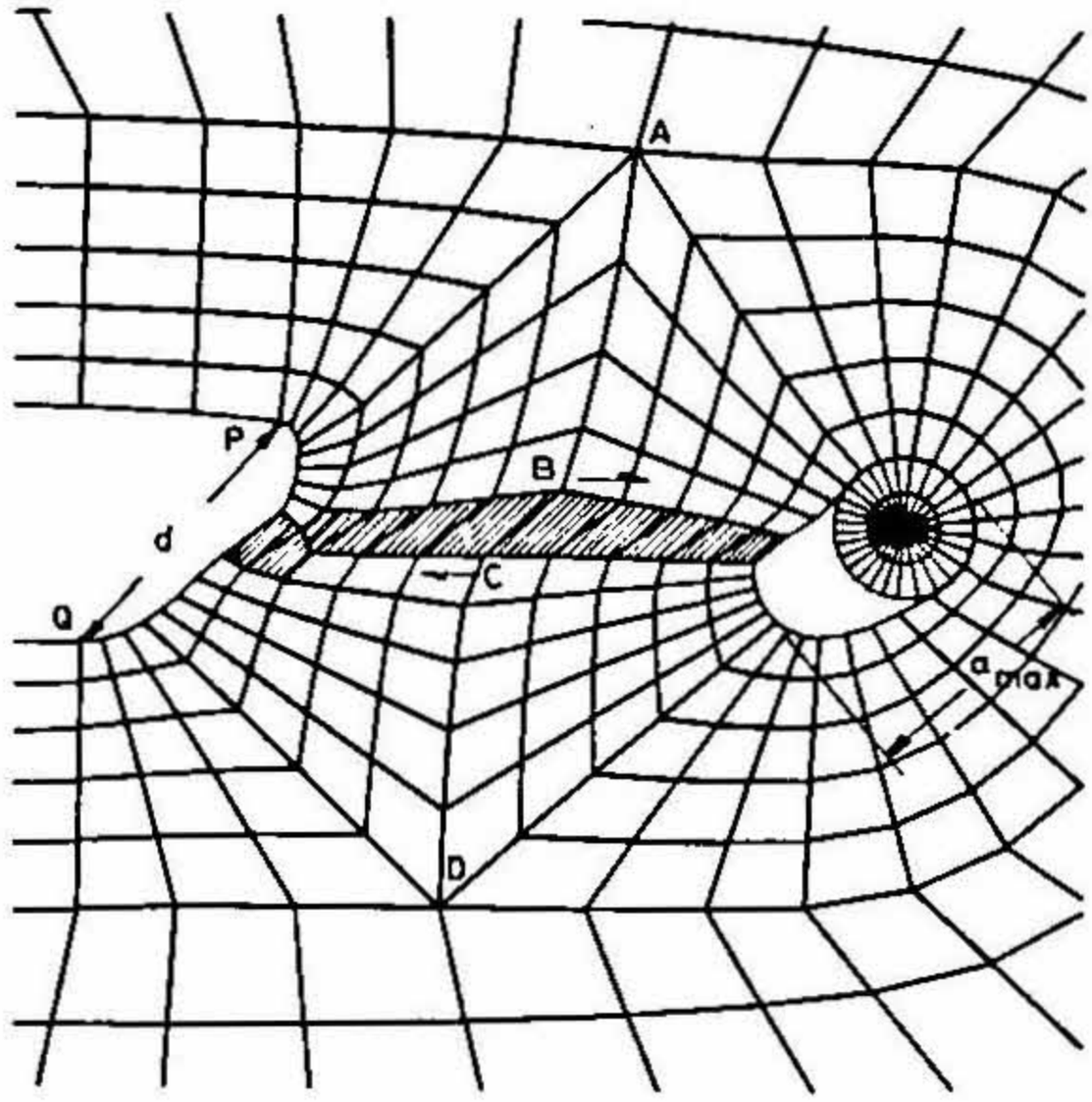

FIG. 9. Deformed mesh near the notch tip and the hole that has grown around the inclusion from the first set of simulations for $\psi = 30°$ at $J/(\sigma_0 L_0) = 0.258$ ($d/b_0 = 2.09$). The failed elements are hatched.

of diameter $a_0 = b_0$ was placed as indicated in Fig. 8. The inclusion was assumed to be rigid (*i.e.*, with a fictitiously high elastic modulus). The objective of this model was to simulate the initiation of a hole by a debonding process around the inclusion and its interaction with the notch tip under mixed-mode loading. To this end, a simple linear constitutive model was chosen to represent the interface between the inclusion and the surrounding metal matrix (see Ghosal[23] for details).

In order to investigate the effect of the bond strength of the above matrix-inclusion interface on mixed-mode ductile fracture initiation, two sets of simulations were conducted by Ghosal and Narasimhan[10]. In the first set, the strain-hardening exponent of the matrix material was chosen as 10. Also, the critical normal stress, σ_c and the ratio α of the critical tangential stress to normal stress of the interface were taken as 2.5 σ_0 and 0.6, respectively. In the second set, $n = 7$, $\sigma_c = 3.5\ \sigma_0$ and $\alpha = 4$ were employed, so that tangential separation at the interface was completely suppressed, and only normal debonding with a higher critical normal stress was permitted. The finite-element analyses were carried out till the stage when the entire ligament connecting the notch tip and the hole that has grown around the inclusion experienced material failure. This stage was taken to signify fracture initiation as suggested by Rice and Johnson[27].

The deformed mesh near the notch tip and the inclusion corresponding to the mixed-mode case $\psi = 30°$ from the first set of simulations is presented in Fig. 9 at a value of normalized loading parameter $J/(\sigma_0 L_0) = 0.258$. As in Fig. 3, it can be seen in Fig. 9 that under mixed-mode loading, the bottom portion of the notch blunts, while the top part sharpens. The notch tip deformation length, which is the linear distance between

points P and Q in Fig. 9, is 2.09 b_0. In Fig. 9, a large hole that has grown around the inclusion after debonding occurs at the matrix-inclusion interface can be perceived. For this set of simulations, debonding commenced very early in the loading history (at around $J/(\sigma_0 L_0) = 0.05$). The results showed that for the Mode I case, the shape of the hole is almost circular, although it becomes slightly oblate in the x_1 direction (see Ghosal and Narasimhan[10]). On the other hand, it can be observed from Fig. 9 that for the mixed-mode case $\psi = 30°$, the hole is skewed and also elongated which is attributed to the large shear stresses in the ligament.

At the stage represented in Fig. 9, the entire ligament connecting the notch tip and the hole has just experienced material failure by micro-void coalescence. The particular elements that have failed are shown hatched. It is important to note in Fig. 9 that large shearing has taken place across the row of failed elements in the direction of the arrows shown. This can be further understood by examining the deformation of the segment BC of the line ABCD which is vertical in the undeformed configuration and is marked as $A_0B_0C_0D_0$ in Fig. 8. It is clear from the above discussion that in the present simulations, the coalescence of the hole (which forms around the large size inclusion) with the notch tip has taken place *via* a void sheet rather than by their direct impingement. In other words, the process of growth of the hole and deformation of the notch has been interrupted by sudden failure of the ligament by porosity formation.

The contours of matrix plastic strain, ε_m^p, for the mixed-mode case $\psi = 30°$ at $J/(\sigma_0 L0) = 0.258$ ($d/b_0 = 2.09$) in a detailed region surrounding the deformed notch and hole are shown in Fig. 10. These contours are taken from the first set of simulations. The inclusion is shown hatched in this figure in order to clearly visualize the hole that has formed and grown around it. It can be seen from Fig. 10 that a band of intense plastic strain has formed in the ligament connecting the blunted part of the notch with the hole. The failed elements shown hatched in Fig. 9 are located within the corridor formed by contours C in Fig. 10. Further, it should be observed that the magnitude of ε_m^p near the sharpened part of the notch (adjacent to point P) is small.

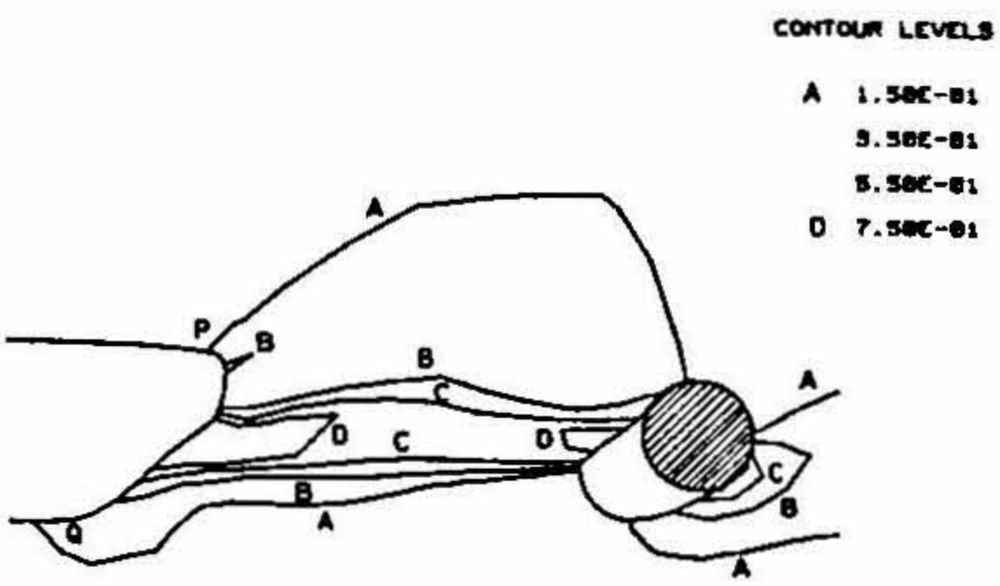

FIG. 10. Contours of ε_m^p near the notch tip and the hole from the first set of simulations for $\psi = 30°$ at $J/(\sigma_0 L_0) = 0.258$ ($d/b_0 = 2.09$).

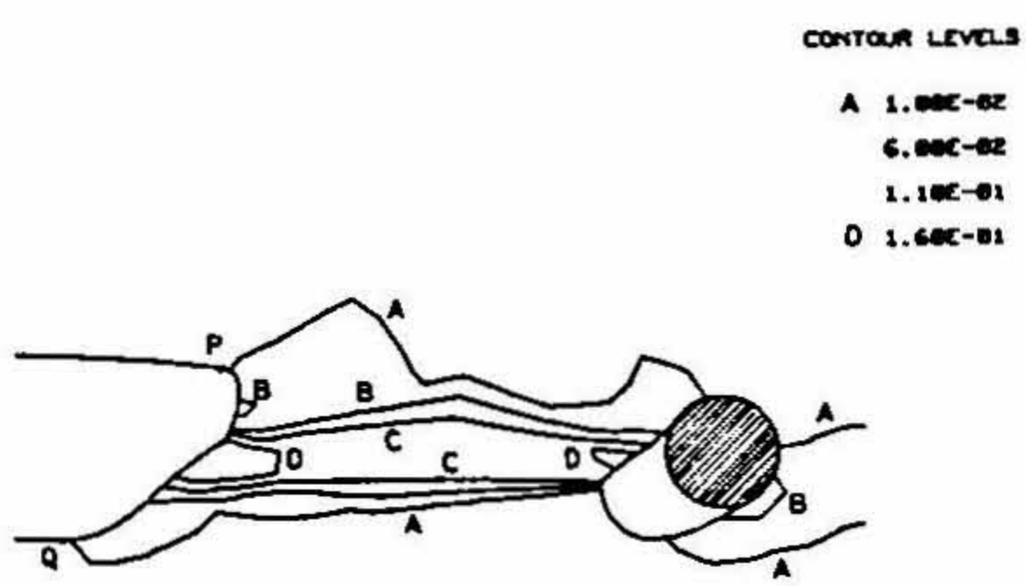

FIG. 11. Contours of void volume fraction f near the notch tip and the hole from the first set of simulations for $\psi = 30°$ at $J/(\sigma_0 L_0) = 0.258$ ($d/b_0 = 2.09$).

The contours of void volume fraction, f, for $\psi = 30°$ at the same stage of deformation as Fig. 10 are presented in Fig. 11. It can be seen from this figure that the contours of void volume fraction are qualitatively similar to the plastic strain contours shown in Fig. 10. This is because micro-void nucleation in the ligament connecting the blunted part of the notch with the hole is triggered by the concentration of plastic strain after the notch and hole have deformed to some extent. Further, micro-void growth in this region is supported by a good combination of plastic strain and triaxial tension. This leads to ductile damage that occurs in a somewhat narrow zone (see region within contour C in Fig. 11) which bridges the ligament. The phenomenon discussed above corresponds to the classic void sheet mechanism, which has been observed in experimental studies (see, for example, Cox and Low[1]) involving materials with two sets of void-nucleating particles of vastly different sizes.

The evolution of the maximum diameter, a_{max}, of the hole which has formed after initiating around the rigid inclusion ahead of the notch tip (see Fig. 9), normalized by the inclusion diameter a_0, is plotted in Figs 12a and b as a function of the normalized loading parameter $J/(\sigma_0 L_0)$ for the first and second set of simulations, respectively. Results are presented in these figures corresponding to different mode-mixities. It should be noted from these figures that during the initial phase of loading, a_{max} remains constant at a_0, and begins to increase only beyond a certain value of $J/(\sigma_0 L_0)$. This delay in evolution of a_{max} is caused by the fact that debonding takes place only when the normal or tangential stress at the matrix-inclusion interface attains a preset critical value. For the first set of analyses to which Fig. 12a pertains, debonding occurred very early for all cases of mode-mixity, because the critical interfacial strengths were not high. Further, as noted earlier, for the pure Mode I case, the hole became oblate in the x_1 direction (Fig. 8). Hence, for this case, the variation of a_{max}/a_0 as well as the normalized longitudinal diameter a_l/a_0 (*i.e.*, in the x_2 direction) with $J/(\sigma_0 L_0)$ are displayed in Fig. 12a. For all other mixed-mode cases shown in Fig. 12a, the hole became elongated along an inclined axis (see, for example, Fig. 9).

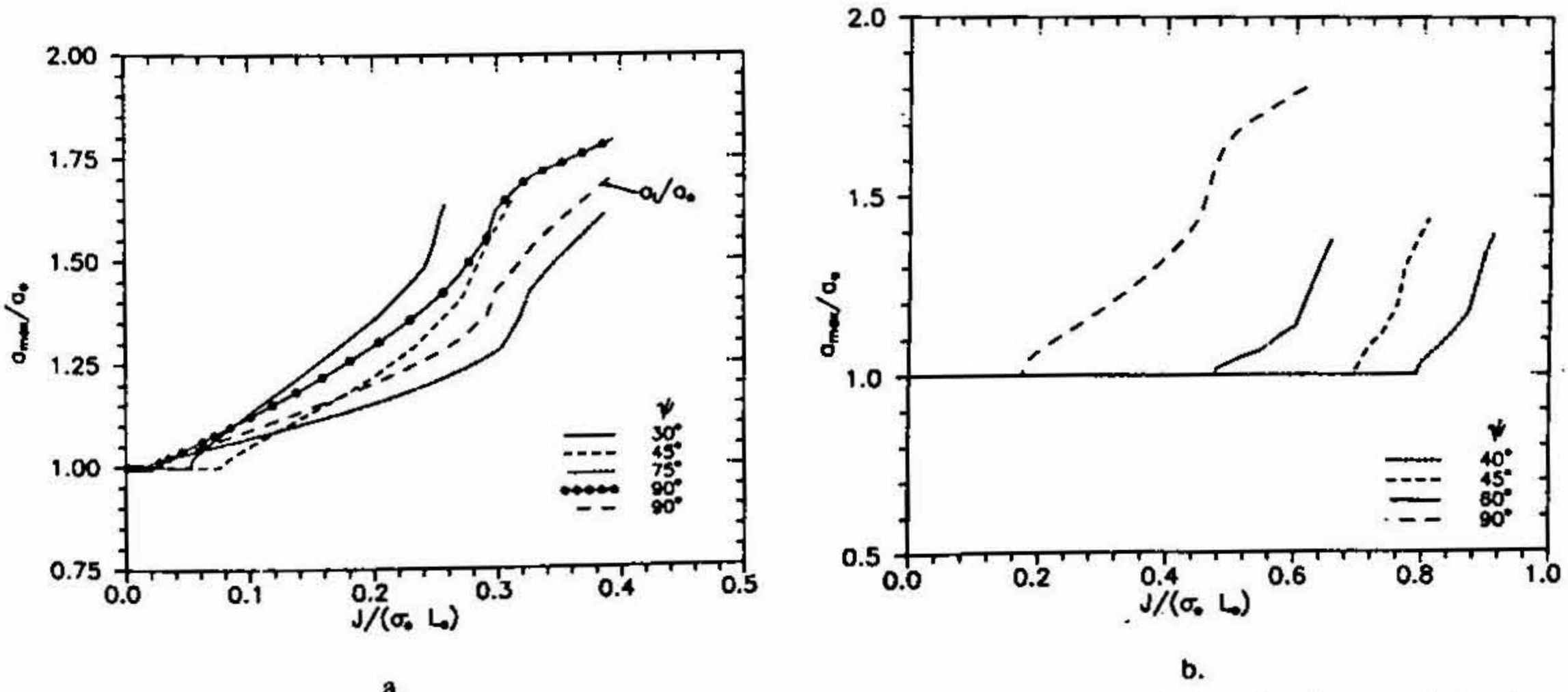

a. b.

FIG. 12a. Evolution of the normalized maximum hole diameter a_{max}/a_0 with $J/(\sigma_0 L_0)$ from the first set of simulations for four cases of mode-mixity. b. Evolution of the normalized maximum hole diameter a_{max}/a_0 with $J/(\sigma_0 L_0)$ from the second set of simulations for four cases of mode-mixity.

It can be observed from Fig. 12a that in the post-debonding phase, the average evolution rate of a_{max} with respect to the loading parameter $J/(\sigma_0 L_0)$ decreases as ψ is reduced initially from 90°. It reaches a minimum at around $\psi = 75°$ and thereafter increases for further reduction in ψ. The above trends are rationalized as follows. As ψ is initially reduced from 90°, there is a reduction in hydrostatic tension around the hole which slows down the growth rate of the hole. However, as ψ decreases below 75°, early localization of plastic strains in the ligament accompanied by strong shear deformation (as can be seen in Fig. 9) takes place. This leads to an increase in the growth rate of the maximum diameter of the hole and it also tends to make the hole highly elongated.

For the second set of simulations, the critical interfacial strengths were chosen to be higher than in the first set. As a consequence, it can be observed from Fig. 12b that debonding happens at higher values of $J/(\sigma_0 L_0)$. Also, unlike in Fig. 12a, it can be seen from Fig. 12b that the above value of $J/(\sigma_0 L_0)$ (at which debonding occurs) increases significantly with reduction in ψ from 90°. This can be easily observed from the delay in evolution of a_{max}/a_0 in the curves displayed in Fig. 12b. As a consequence, for this set of simulations, a_{max}/a_0, for a given $J/(\sigma_0 L_0)$, decreases strongly as ψ is reduced from 90°. Further, as noted by Ghosal and Narasimhan[10], due to the above delay in debonding, the failure of the ligament connecting the notch tip with the inclusion by micro-void coalescence is also slowed down with reduction in ψ from 90°.

Ghosal and Narasimhan[10] also observed that for the first set of simulations, the value of the normalized notch tip deformation length d/b_0 at fracture initiation by micro-void coalescence in the ligament was practically independent of mode-mixity ψ (similar to that noted from Fig. 4 in Section 3.1). On the other hand, for the second set of simulations (with higher critical interfacial strengths), the notch tip deformation length at fracture initiation was not a constant, but increased significantly with reduction in ψ from 90°. Thus, the above quantity retains its significance as a local fracture characterizing parameter for mixed-mode loading only for materials with loosely bonded inclusions (*i.e.*, with low interfacial strengths).

3.3 *Mixed-mode fracture initiation in a ductile material with a dual population of second-phase particles*

Ghosal and Narasimhan[11] conducted numerical simulations with a view to study the mixed-mode ductile fracture mechanisms taking into account void initiation at a dual distribution of second-phase particles of vastly different sizes. The initiation of voids at small, uniformly distributed particles was assumed to be based on a strain-controlled mechanism. This was implemented through the first term in the right-hand side of the void nucleation law eqn (6) and by employing eqn (7) for $\mathcal{A}$, wherein f_n was taken as a constant with a value of 0.04. On the other hand, a stress-controlled void nucleation law was used within the framework of the Gurson model for simulating formation of voids at large inclusions. This is because the analysis of Argon *et al.*[22] suggests that a critical (matrix-inclusion) interfacial stress can be used for void nucleation by inclusion debonding (see also Section 3.2). This was incorporated in the constitutive model through the second term in the right-hand side of eqn (6) and by employing eqn (8) for $\mathcal{B}$.

In order to capture the discrete nature of void initiation at the sites of large-size particles, they were modelled as *islands* (*i.e.*, as contours which enclose the centre of the particles) of the amplitude $\hat{f}_n$ of the stress-controlled void nucleation function (8a) (see Narasimhan[13] for details). Thus, considering the large particles to be distributed in a rectangular array and to be circular-cylindrical in shape, the spatial variation of the function $\hat{f}_n$ in the plane of deformation is assumed as:

$$\hat{f}_n = \begin{cases} a & 0 \le r \le r_0 \\ a \exp(\beta - \beta r^2 / r_0^2) & r > r_0. \end{cases} \tag{9}$$

Here, r is the radial distance measured from the centre of a particle, r_0, its radius, and β, a constant taken as less than unity which controls the decay rate of the exponential function in (9). The amplitude a is chosen based on a unit cell model (see Narasimhan[13]), so that $\hat{f}_n$ is consistent with the radius of the particle r_0 and the inter-particle spacing L_0.

The 2D plane strain, mixed-mode small-scale yielding problem was modelled in a similar fashion as in Sections 3.1 and 3.2. The radius r_0 of the large size particles was taken as 0.3 b_0 and their centre-to-centre spacing L_0 was chosen as 3 b_0, where b_0 is the initial notch diameter. Also, the decay parameter β in (9) was taken as 0.2. In order to illustrate the distribution of the large synthetic *inclusions* around the notch tip, the contours of $\hat{f}_n = 0.05$ are shown in Fig. 13. These contours, especially those far away from the notch tip, do not have the circular shape expected from (9) because of the discretization introduced by finite elements. The average size of one of the closed contours in Fig. 13 is roughly three times the size of the particle that is being simulated. In order to

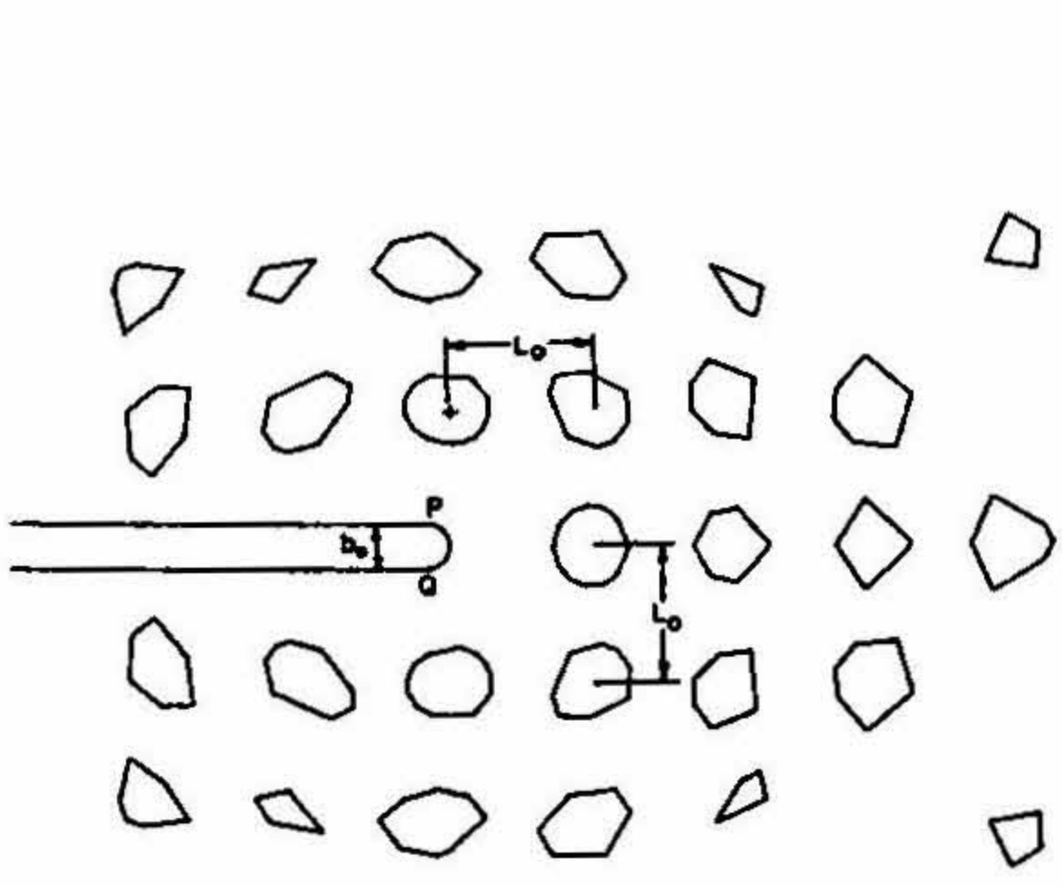

FIG. 13. Contours of $\hat{f}_n = 0.05$ illustrating the distribution of the synthetic inclusions around the notch.

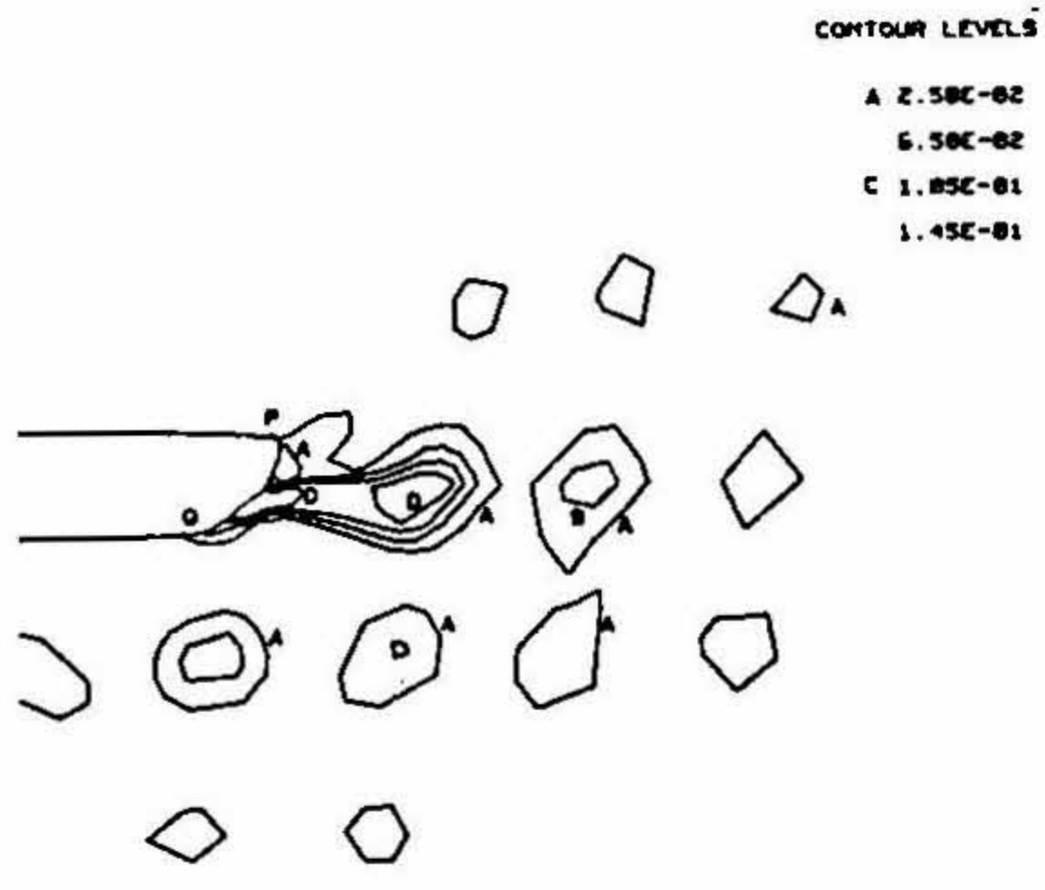

FIG. 14. Contours of void volume fraction for $\psi = 30°$ at $J/(\sigma_0 L_0) = 0.511$ ($d/b_0 = 2.29$) obtained from the analysis with $\sigma_N = 1.75\ \sigma_0$ and $n = 10$.

investigate the effect of the nucleation stress σ_N (see eqn (8)) and the matrix strain-hardening exponent n (see eqn (3)) on fracture initiation, several sets of simulations were carried out by Ghosal and Narasimhan[11] by taking different values for these parameters. The most important results from their work are presented below.

The contours of void volume fraction for the mixed-mode case $\psi = 30°$ from one of the analyses of Ghosal and Narasimhan[11] is displayed in Fig. 14. For this analysis, σ_N and n were chosen as 1.75 σ_0 and 10, respectively. This figure corresponds to the stage of loading when $J/(\sigma_0 L_0) = 0.511$ ($d/b_0 = 2.29$). The islands, in the form of closed concentric contours, in this figure have developed around the *synthetic inclusion* sites (*i.e.*, the void nucleating sites). It can be seen that porosity has formed around the synthetic inclusions over a wide region surrounding the notch tip, but it is restricted mainly to the lower half-region adjacent to the blunted part of the notch tip. This is because stress triaxiality is very low at the sharpened part of the notch (see Fig. 5b), and, hence, the nucleation stress at the inclusion sites near this part of the notch (upper half-region in Fig. 14) is not attained.

At the stage represented in Fig. 14, the entire ligament connecting the blunted part of the notch and the first synthetic inclusion site ahead of it has experienced failure by micro-void coalescence. As in Section 3.2, this is taken to signify fracture initiation (see Rice and Johnson[27]). This is activated by the concentration of plastic strain in the above ligament after porosity accumulates at the notch tip and the first synthetic inclusion. This phenomenon triggers plastic strain-controlled void nucleation at the small-size particles in the ligament leading to its failure.

The value of the normalized loading parameter $J/(\sigma_0 L_0)$ at which fracture initiation occurs is plotted as a function of the mode-mixity angle ψ in Figs 15 and 16. In Fig. 15, the results from analyses with low nucleation stress σ_N are presented, whereas those from analyses carried out with higher nucleation stress are shown in Fig. 16. In each of these figures, results obtained from computations with two values of strain-hardening exponent n are displayed. In Fig. 15, for the analysis with $\sigma_N = 1.75\ \sigma_0$ and $n = 10$, the variation of $J/(\sigma_0 L_0)$ at fracture initiation with ψ is shown corresponding to failure of the ligament by micro-void coalescence as well as by shear crack propagation. On the other hand, for all other analyses, only simulations of failure in the ligament by micro-void coalescence were performed, and the results are presented in Figs 15 and 16.

It can be observed from Fig. 15 that for the analyses with low σ_N, the critical value of J based on the micro-void coalescence mechanism decreases as ψ is reduced from 90°, reaches a minimum between $\psi = 45°$ and 30°, and thereafter increases for further reduction in ψ. As a consequence of this increase, it is found from Fig. 15 that for the analysis with $\sigma_N = 1.75\ \sigma_0$ and $n = 10$, the above curve crosses over the curve that delineates material failure by shear localization at around $\psi = 15°$. Thus, it may be concluded that micro-void coalescence in the ligaments between the notch tip and nearby inclusions is the governing failure mechanism for ψ in the range from 90° to 15°. On the other hand, failure by shear localization from the sharpened part of the notch will precede that due to micro-void coalescence for $\psi < 15°$.

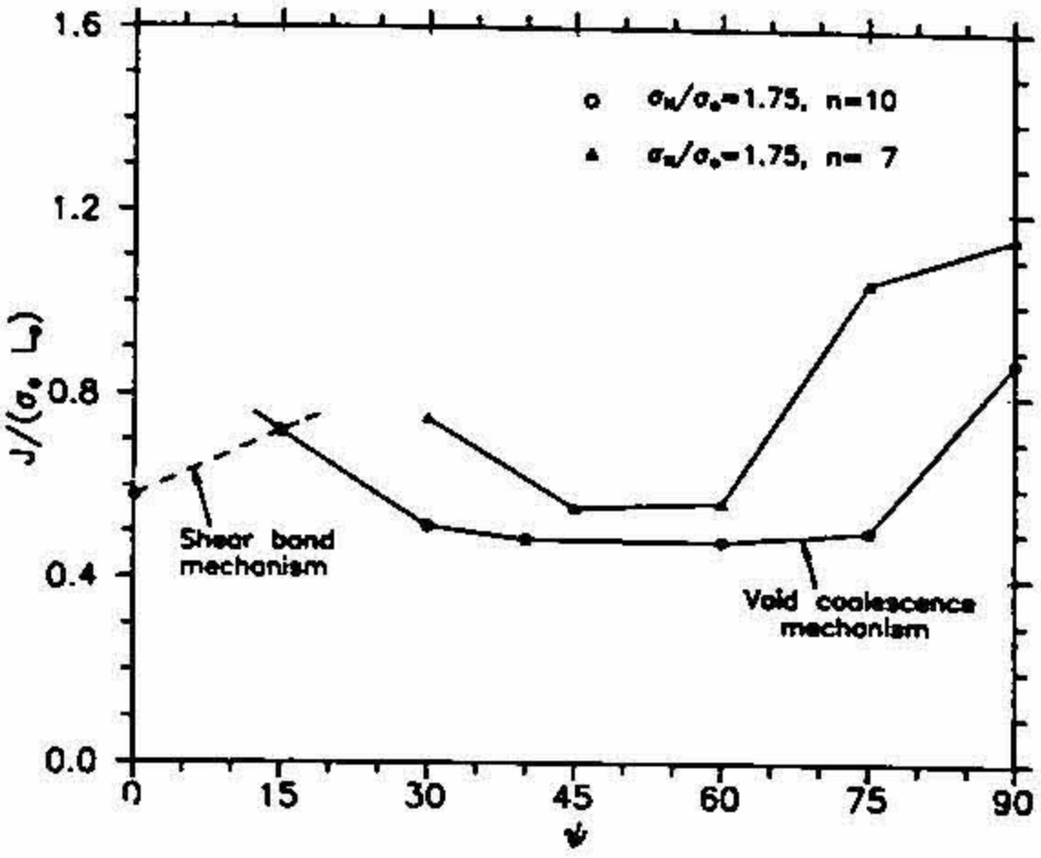

FIG. 15. Variation of $J/(\sigma_0 L_0)$ at fracture initiation with mode-mixity angle ψ for analyses with low nucleation stress.

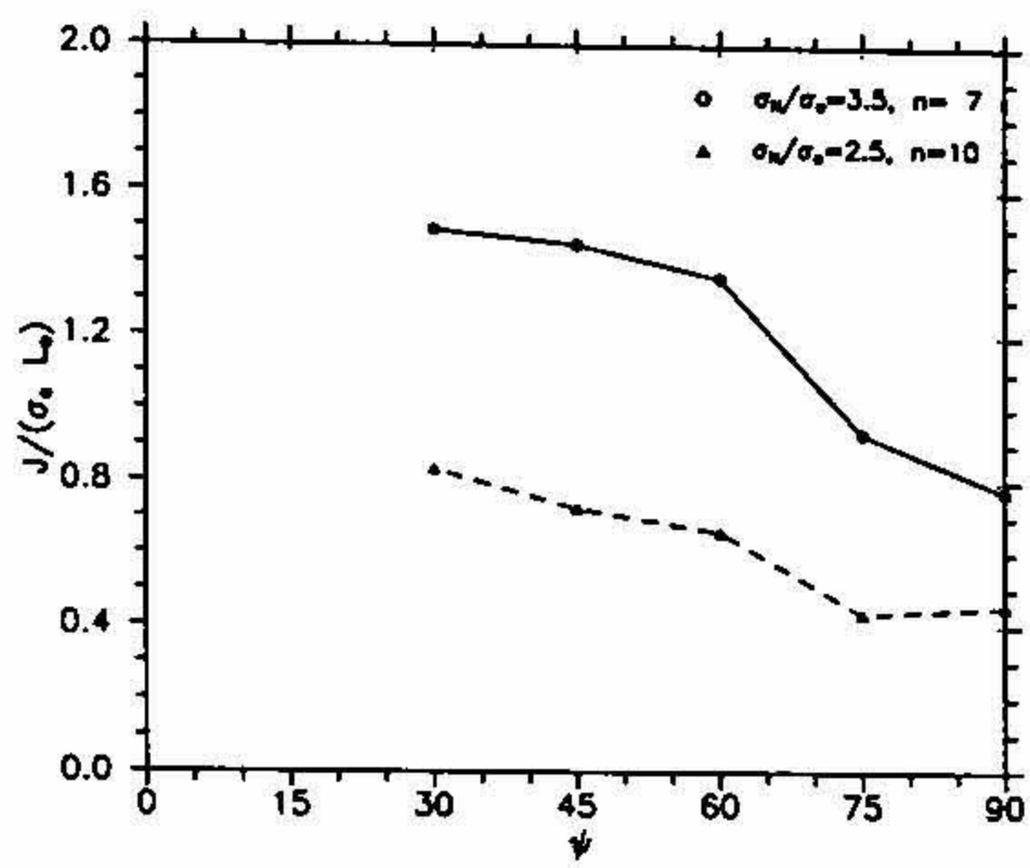

FIG. 16. Variation of $J/(\sigma_0 L_0)$ at fracture initiation with mode-mixity angle ψ for analyses with high nucleation stress.

The above observations are essentially the same as that made by Ghosal and Narasimhan[10] for a *loosely bonded inclusion*. Thus, for the cases shown in Fig. 15, porosity development at the inclusion sites near the notch tip begins early in the loading history. As explained by Ghosal and Narasimhan[10,11], the reason for the above trends of the failure curves (in Fig. 15) is attributed to the effect of mode-mixity on stress triaxiality and plastic strain accumulation near the notch tip. There is a decrease in the magnitude of hydrostatic tension near the notch tip when ψ is reduced from 90°. On the other hand, faster accumulation of plastic strain occurs in the ligament. As ψ is decreased from 90°, the effect of the latter in promoting void growth and coalescence in the ligament offsets that caused by the reduction in σ_H. This leads to the decrease in the critical value of J with decrease in ψ from 90°. However, for reduction in ψ below 30°, the hydrostatic tension falls to an extremely low level and hinders the growth of the micro-voids that have nucleated within the band of plastic strain concentration in the ligament. This results in an increase in the critical value of J corresponding to failure by micro-void coalescence for ψ less than 30°. The above noted decrease in hydrostatic tension renders failure by micro-void coalescence in the ligament almost impossible for ψ less than 15°. On the other hand, the localization of shear deformation in a narrow band from the sharpened part of the notch facilitates the propagation of a shear crack for $0 \leq \psi \leq 15°$.

Finally, it must be mentioned that the failure curve pertaining to $n = 7$ is above that for $n = 10$ in Fig. 15. This is because, although the nucleation stress at the synthetic inclusion sites near the notch tip is attained earlier for $n = 7$ (because of the higher magnitude of stresses around the notch tip), continued development of porosity around these inclusions is slow (with respect to the loading parameter $J/(\sigma_0 L_0)$) because of higher strain hardening. This results in higher magnitude of $J/(\sigma_0 L_0)$ at fracture initiation for $n = 7$ as compared to the case $n = 10$. In this context, it must be mentioned that Thomason[20] has found, on the basis of an approximate integration of Rice and Tracey's[28] equations, that the presence of strain hardening slows down the growth of a spherical void in a ductile matrix.

The trends displayed by the failure curves shown in Fig. 15 resemble the experimental results of Tohgo *et al.*[4] for SM41A steel and those of Maiti and Mahanty[6] for an aluminium alloy. Ghosal and Narasimhan[9] extracted the variation of the critical value of J at failure initiation with ψ from the experimental data given by Tohgo *et al*[4]. These results which were presented in Fig. 11 of Ghosal and Narasimhan[9] exhibit the general features seen in Fig. 15. Thus, the decrease in the critical value of J as ψ is reduced from 90°, and the crossover of the curves depicting failure by the two mechanisms can be observed in these experimental results.

On examining Fig. 16, it can be seen that the failure curves for the analyses wherein the nucleation stress at the inclusion sites was chosen to be high, show an increase in $J/(\sigma_0 L_0)$ at fracture initiation with reduction in ψ from 90°. These curves confirm the features observed in the work of Ghosal and Narasimhan[10] for an inclusion which is *strongly bonded* to the matrix. The increase in the value of $J/(\sigma_0 L_0)$ at fracture initiation with reduction in ψ in Fig. 16 is an outcome of the delayed onset of porosity formation at the synthetic inclusion sites when the Mode II component is increased. This is tied to the fact that the stress levels around the notch decrease as ψ is reduced from 90° (see, for example, Figs 5a and b) making it more difficult to attain the high value of the nucleation stress chosen in the analyses reported in Fig. 16. The localization of plastic strain in the ligaments connecting the synthetic inclusions is also retarded because of this reason which, in turn, slows down failure by micro-void coalescence. The failure curves depicted in Fig. 16 resemble the behaviour reported by Aoki *et al.*[5] for an aluminium alloy and Maccagno and Knott[7] for HY130 steel.

4. Concluding remarks

It is clear from the above overview that the numerical simulations of Ghosal and Narasimhan[9-11] have helped in understanding some important issues connected with mixed-mode ductile fracture initiation. The following are the main conclusions of these studies.

1. It was found from the analyses conducted by Ghosal and Narasimhan[9] that under mixed-mode loading, one portion of the notch surface blunts, while the remaining part sharpens. Further, for Mode I-predominant loading, failure by micro-void coalescence always occurs at the blunted part of the notch, whereas for loading close to Mode II, shear localization takes place near the sharpened part of the notch. The simulated failure zones resemble those observed in the experiments.

2. In Ghosal and Narasimhan[10], the initiation of a hole by debonding around a circular-cylindrical inclusion ahead of a notch and its interaction with the notch tip under mixed-mode loading were modelled. The results showed that while the hole is almost circular for Mode I loading, with some oblateness perpendicular to the loading axis, it becomes highly elongated along an inclined axis for Mode II type loading. When the matrix-inclusion bond strength is low, early debonding takes place at the inclusion surface. Further, for this case, the average growth rate of the maximum hole diameter with respect to the normalized loading parameter $J/(\sigma_0 L0)$ decreases initially as ψ is reduced from 90° (Mode I), but thereafter increases significantly for

reduction in ψ below 75°. Also, for this case, the notch tip deformation length at fracture initiation (associated with complete failure of the ligament between the notch tip and the inclusion) by micro-void coalescence is almost independent of mode-mixity for ψ in the range 30 to 90°. It can thus be viewed as a local fracture characterizing parameter for this case. On the other hand, when the matrix-inclusion bond strength is high, there is considerable delay in debonding at the inclusion surface as ψ is reduced from 90°.

3. The results from Ghosal and Narasimhan[11] showed that when the nucleation stress at large inclusions is low (*i.e.*, when the inclusions are loosely bonded), the critical value of J at fracture initiation decreases as ψ is reduced from 90°. On the other hand, when the nucleation stress is high (*i.e.*, when the inclusions are firmly bonded), it increases as ψ is reduced from 90°.

The last conclusion made above provides a possible explanation for the different experimentally observed trends in the variation of fracture toughness *versus* mode-mixity in ductile alloys. However, there are other factors that have not been investigated in Ghosal and Narasimhan[9–11] which can also influence this variation. These include 3D effects and the influence of large scale yielding in finite width geometries, which can affect the stress and deformation fields near the crack tip. The investigation of these issues, along with direct comparisons with experimental results, needs to be taken up for future studies.

Acknowledgement

RN is grateful to the Aeronautics Research and Development Board, Government of India, for financial support under sponsored project No.Aero/RD-134/100/10/91-95/634, which made the investigations reported here possible.

References

1. Cox, T. B. and Low, J. R. — An investigation of the plastic fracture of AISI 4340 and 18 nickel-200 grade maraging steels, *Metall.Trans.*, 1974, 5, 1457–1470.

2. Hahn, G. T. and Rosenfield, A. R. — Metallurgical factors affecting fracture toughness of aluminium alloys, *Metall. Trans. A*, 1975, 6, 653–658.

3. Otsuka, A., Tohgo, K. and Okamato, Y. — Relationship between ductile crack initiation and void volume fraction. *Nucl. Engng Des.*, 1987, 105, 121–129.

4. Tohgo, K., Otsuka, A. and Gao, H.W. — The behaviour of ductile crack initiation from a notch under mixed-mode loading, *Proc. Far East Fracture Group Workshop* (M. Sakata, ed.), Tokyo Inst. Tech., Japan, 1988, pp. 101–108.

5. Aoki, S. *et al.* — Elastic-plastic fracture behaviour of an aluminium alloy under mixed-mode loading, *J. Mech. Phys. Solids*, 1990, 35, 195–213.

6. Maiti, S. K. and Mahanty, D. K — Experimental and finite element studies on mode I and mixed-mode (I and II) stable crack growth-II. Finite element analysis, *Engng Fracture Mech.*, 1990, 37, 1251–1275.

7. MACCAGNO, T. M. AND KNOTT, J. F. The mixed mode I/II fracture behaviour of lightly tempered HY130 steel at room temperature, *Engng Fracture Mech.*, 1992, **41**, 805–820.

8. RICE, J. R. A path independent integral and the approximate analysis of strain concentration by notches and cracks, *J. Appl. Mech.*, 1968, **35**, 379–386.

9. GHOSAL, A. K. AND NARASIMHAN, R. A finite element analysis of mixed-mode fracture initiation by ductile failure mechanisms, *J. Mech. Phys. Solids*, 1994, **42**, 953–978.

10. GHOSAL, A. K. AND NARASIMHAN, R. A finite element study of the effect of void initiation and growth mixed-mode ductile fracture, submitted to *J. Mech. Phys. Solids*, 1995.

11. GHOSAL, A. K. AND NARASIMHAN, R. Mixed-mode fracture initiation in a ductile material with a dual population of second-phase particles, *Mater. Sci. Engng A*, 1995 (in press).

12. GURSON, A. L. Continuum theory of ductile rupture by void nucleation and growth: Part I–Yield criteria and flow rules for porous ductile materials, *J. Engng Mat. Technol.*, 1977, **99**, 2–15.

13. NARASIMHAN, R. A numerical study of fracture initiation in a ductile material containing a dual population of second-phase particles-I. Static loading, *Engng Fracture Mech.*, 1994, **47**, 919–934.

14. TVERGAARD.V. AND NEEDLEMAN, A. Analysis of cup-cone fracture in a round tensile bar, *Acta Metall.*, 1984, **32**, 157–169.

15. TVERGAARD, V. Influence of voids on shear band instabilities under plane strain conditions, *Int. J. Fracture*, 1981, **17**, 389–407.

16. BROWN, L. M. AND EMBURY, J. D. The initiation and growth of voids at second-phase particles. In *Microstructure and design of alloys*, 1973, pp. 164–179, Cambridge.

17. ANDERSSON, H. Analysis of a model for void growth and coalescence ahead of a moving crack tip, *J. Mech. Phys. Solids*, 1977, **25**, 217–233.

18. GURSON, A.L. Porous rigid-plastic materials containing rigid inclusions: Yield function, plastic potential and void nucleation. In *Proc. Int. Conf. on Fracture* (D.M.R.Taplin, ed.), Vol. 2A, 1977, pp. 357–364, Pergamon.

19. NEEDLEMAN, A. AND RICE, J.R. Limits to ductility set by plastic flow localization. In *Mechanics of sheet metal forming* (D. P. Koistinen and N. M. Wang, eds), 1978, pp. 237–267, Plenum.

20. THOMASON, P. F. *Ductile fracture of metals*, 1990, Pergamon.

21. CHU, C. C. AND NEEDLEMAN, A. Void nucleation effects in biaxially stretched sheets, *J. Engng Mat. Technol.*, 1980, **102**, 249–256.

22. ARGON, A. S., IM, J. AND SAFOGULU, R. Cavity formation from inclusions in ductile fracture, *Metall. Trans. A.*, 1975, **6**, 825–837.

23. GHOSAL, A.K. *Numerical simulations of mixed-mode ductile fracture initiation*, Ph. D. Thesis, Indian Institute of Science, Bangalore, India, 1995.

24. TVERGAARD, V. Influence of void nucleation on ductile shear fracture at a free surface, *J. Mech. Phys. Solids*, 1982, **30**, 399–425.

25. RICE, J.R. Mathematical analysis in the mechanics of fracture. In *Fracture: An advanced treatise* (H. Liebowitz, eds), Vol. 2, 1968, pp. 191–311, Academic Press.

26. SYMINGTON, M., SHIH, C. F. AND ORTIZ, M. *Tables of plane strain mixed-mode plastic crack tip fields*, Brown University report, Providence, USA, 1988.

27. RICE, J. R. AND JOHNSON, M. A. The role of large crack tip geometry changes in plane strain fracture. In *Inelastic behaviour of solids* (M. F. Kanninen *et al.*, eds), 1970, pp. 641–672, McGraw–Hill,

28. RICE, J. R. AND TRACEY, D. M On the ductile enlargement of voids in triaxialstress fields, *J. Mech. Phys. Solids*, 1968, 17, 201–217.